

# Spatio-temporal correlations and visual signalling in a complete neuronal population

Jonathan W. Pillow<sup>1</sup>, Jonathon Shlens<sup>2</sup>, Liam Paninski<sup>3</sup>, Alexander Sher<sup>4</sup>, Alan M. Litke<sup>4</sup>, E. J. Chichilnisky<sup>2</sup> & Eero P. Simoncelli<sup>5</sup>

Statistical dependencies in the responses of sensory neurons govern both the amount of stimulus information conveyed and the means by which downstream neurons can extract it. Although a variety of measurements indicate the existence of such dependencies<sup>1–3</sup>, their origin and importance for neural coding are poorly understood. Here we analyse the functional significance of correlated firing in a complete population of macaque parasol retinal ganglion cells using a model of multi-neuron spike responses<sup>4,5</sup>. The model, with parameters fit directly to physiological data, simultaneously captures both the stimulus dependence and detailed spatio-temporal correlations in population responses, and provides two insights into the structure of the neural code. First, neural encoding at the population level is less noisy than one would expect from the variability of individual neurons: spike times are more precise, and can be predicted more accurately when the spiking of neighbouring neurons is taken into account. Second, correlations provide additional sensory information: optimal, model-based decoding that exploits the response correlation structure extracts 20% more information about the visual scene than decoding under the assumption of independence, and preserves 40% more visual information than optimal linear decoding<sup>6</sup>. This model-based approach reveals the role of correlated activity in the retinal coding of visual stimuli, and provides a general framework for understanding the importance of correlated activity in populations of neurons.

How does the spiking activity of a neural population represent the sensory environment? The answer depends critically on the structure of neuronal correlations, or the tendency of groups of neurons to fire temporally coordinated spike patterns. The statistics of such patterns have been studied in a variety of brain areas, and their significance in the processing and representation of sensory information has been debated extensively<sup>2,3,7–13</sup>.

Previous studies have examined visual coding by pairs of neurons<sup>11</sup> and the statistics of simultaneous firing patterns in larger neural populations<sup>14,15</sup>. However, no previous approach has addressed how correlated spiking activity in complete neural populations depends on the pattern of visual stimulation, or has answered the question of how such dependencies affect the encoding of visual stimuli.

Here we introduce a model-based methodology for studying this problem. We describe the encoding of stimuli in the spike trains of a neural population with a generalized linear model (Fig. 1a), a generalization of the well-known linear–nonlinear–Poisson (LNP) cascade model<sup>4,5,16,17</sup>. In this model, each cell's input is described by a set of linear filters: a stimulus filter, or spatio-temporal receptive field; a post-spike filter, which captures dependencies on spike-train history

(for example, refractoriness, burstiness and adaptation); and a set of coupling filters, which capture dependencies on the recent spiking of other cells. For each neuron, the summed filter responses are exponentiated to obtain an instantaneous spike rate. This is equivalent to exponentiating the filter outputs and then multiplying; the exponentiated post-spike and coupling filters (as plotted in Fig. 1) may therefore be interpreted as spike-induced gain adjustments of the neuron's firing rate.

Although this model is strictly phenomenological, its components can be loosely compared to biophysical mechanisms: the stimulus filter approximates the spatio-temporal integration of light in the outer retina and passive dendritic filtering; the post-spike filter mimics voltage-activated currents following a spike; coupling filters resemble synaptic or electrical interactions between cells (and can mimic the effects of shared input noise); and the exponential non-linearity implements a 'soft threshold', converting membrane potential to instantaneous spike probability. Note that the post-spike and coupling filters, which allow stochastic spiking in one cell to affect subsequent population activity, give rise to shared, non-Poisson variability in the model response.

We fit the model to data recorded *in vitro* from a population of 27 ON and OFF parasol ganglion cells (RGCs) in a small patch of isolated macaque monkey retina, stimulated with 120-Hz spatio-temporal binary white noise. The receptive fields of each of the two cell types formed a complete mosaic covering a small region of visual space (Fig. 1b), indicating that every parasol cell in this region was recorded<sup>15,18</sup>. Such complete recordings, which have not been achieved elsewhere in the mammalian nervous system, are essential for understanding visual coding in neural populations.

The model contains many parameters that specify the shapes of all filters, but fitting by maximizing likelihood remains highly tractable<sup>5</sup>. A penalty on coupling filters was used to obtain a minimally sufficient set of coupling filters, which yields an estimate of the network's functional connectivity<sup>19,20</sup>.

Figure 1 shows the estimated filters describing input to example ON and OFF cells. The stimulus filters exhibit centre-surround receptive field organization consistent with previous characterizations of parasol cells. Post-spike filters show the time course of recovery from refractoriness after a spike, and coupling filters show the effects of spikes from nearby cells: for the ON cell (top), spikes in neighbouring ON cells elicit a large, transient excitation (increasing the instantaneous spike rate by a factor of three), whereas spikes in nearby OFF cells elicit suppression. These effects are reversed in the OFF cell, which is excited/suppressed by spikes in neighbouring OFF/ON cells. Both populations exhibit approximate nearest-neighbour connectivity, with coupling strength falling as a function of distance

<sup>1</sup>Gatsby Computational Neuroscience Unit, UCL, 17 Queen Square, London WC1N 3AR, UK. <sup>2</sup>The Salk Institute, 10010 North Torrey Pines Road, San Diego, California 92037, USA. <sup>3</sup>Department of Statistics and Center for Theoretical Neuroscience, Columbia University, 1255 Amsterdam Avenue, New York, New York 10027, USA. <sup>4</sup>Santa Cruz Institute for Particle Physics, University of California, Santa Cruz, 1156 High Street, Santa Cruz, California 95064, USA. <sup>5</sup>Howard Hughes Medical Institute, Center for Neural Science, and Courant Institute of Mathematical Sciences, New York University, 4 Washington Place, Room 809, New York, New York 10003, USA.

between receptive field centres<sup>15</sup>. We found that fitted stimulus filters have smaller surrounds than the spike-triggered average, indicating that a portion of the classical surround can be explained by interactions between cells<sup>21</sup> (see Supplementary Information).

To assess accuracy in capturing the statistical dependencies in population responses, we compared the pairwise cross-correlation function (CCF) of RGCs and simulated model spike trains (Fig. 2). For nearby ON–ON and OFF–OFF pairs, the CCF exhibits a sharp peak at zero, indicating the prevalence of synchronous spikes; however, for ON–OFF pairs, a trough at zero indicates an absence of synchrony. For all 351 possible pairings, the model accurately reproduces the CCF (Fig. 2a–c, e, f).

To examine whether inter-neuronal coupling was necessary to capture the response correlation structure, we re-fitted the model without coupling filters (that is, so that each cell's response depends only on the stimulus and its own spike-train history). This 'uncoupled model' assumes that cells encode the stimulus independently, although correlations may still arise from the overlap of stimulus filters. However, the uncoupled model fails to reproduce the sharp CCF peaks observed in the data. These peaks are also absent from CCFs computed on trial-shuffled data, indicating that fast-timescale correlations are not stimulus-induced and therefore cannot be captured by any independent encoding model.

Higher-order statistical dependencies were considered by inspecting correlations in three-neuron groups: triplet CCFs show the spike rate of one cell as a function of the relative time to spikes in two other cells (Fig. 2e–g)<sup>15</sup>. For adjacent neurons of the same type, triplet CCFs have substantial peaks at zero ('triplet synchrony'), which are well matched by the full model.

Although the full and uncoupled models differ substantially in their statistical dependencies, the two models predict average light responses in individual cells with nearly identical accuracy, capturing 80–95% of the variance in the peri-stimulus time histogram (PSTH) in 26 out of 27 cells (Fig. 3a–c). Both models therefore accurately describe average single-cell responses to new stimuli. However, the full model achieves higher accuracy, predicting multi-neuronal spike responses on a single trial ( $8 \pm 3\%$  more bits per spike, Fig. 3d). This discrepancy can be explained by the fact that noise is shared across

neurons. Shared variability means that population activity carries information about a single cell's response (owing to coupling between cells) beyond that provided by the stimulus alone. Individual neurons therefore appear less noisy when conditioned on spiking activity in the rest of the population than they appear in raster plots.

We measured the effect of correlations on single-trial, single-cell spike-train prediction by using the model to draw samples of a single cell's response given both the stimulus and the spiking activity in the rest of the population on a single trial (Fig. 3e, f). Averaging the resulting raster plot gives a prediction of the cell's single-trial spike rate, or 'population-conditioned' PSTH for a single trial. We compared these predictions with the cell's true spike times (binned at 2 ms) across all trials and found that on nearly every trial, the model-based prediction is more highly correlated with the observed spikes than the neuron's full PSTH (Fig. 3g). Note that the full PSTH achieves the highest correlation possible for any trial-independent prediction. Thus, by exploiting the correlation structure, the coupled model predicts single-neuron spike times more accurately than any independent encoding model.

Although the full model accurately captures dependencies in the activity of RGCs, it is not obvious *a priori* whether these dependencies affect the amount of sensory information conveyed by RGC responses. In principle, the correlation structure could be necessary to predict the responses, but not to extract the stimulus information that the responses carry<sup>13</sup>. To examine this issue directly, we used the full and uncoupled models to perform Bayesian decoding of the population response (Fig. 4a), which optimally reconstructs stimuli given an accurate description of the encoding process. For comparison, we also performed Bayesian decoding under a Poisson (that is, LNP) model and optimal linear decoding<sup>6</sup>.

Each decoding method was used to estimate short (150-ms) segments of the stimulus given all relevant spike times from the full population (Fig. 4b). Bayesian decoding under the coupled model recovers 20% more information than Bayesian decoding under the uncoupled model, indicating that knowledge of the correlation structure is critical for extracting all sensory information contained in the population response. This improvement was invariant to enhancements of the

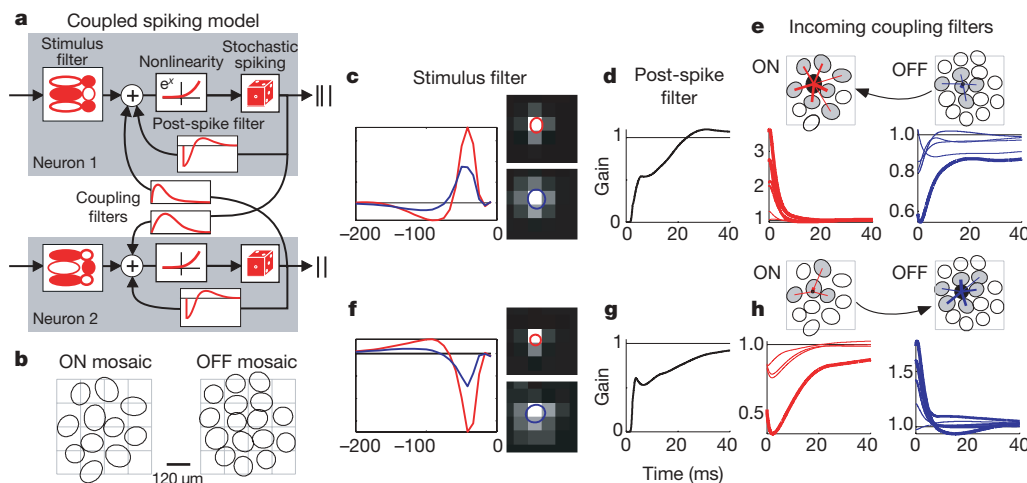


**Figure 1 | Multi-neuron encoding model and fitted parameters.** **a**, Model schematic for two coupled neurons: each neuron has a stimulus filter, a post-spike filter and coupling filters that capture dependencies on spiking in other neurons. Summed filter output passes through an exponential nonlinearity to produce the instantaneous spike rate. **b**, Mosaics of 11 ON and 16 OFF retinal ganglion cell receptive fields, tiling a small region of visual space. Ellipses represent 1 s.d. of a Gaussian fit to each receptive field centre; the square grid indicates stimulus pixels. **c–e**, Parameters for an example ON cell. **c**, Temporal and spatial components of centre (red) and surround (blue) filter components, the difference of which is the full stimulus filter.

**d**, Exponentiated post-spike filter, which may be interpreted as multiplying the spike rate after a spike at time zero. It produces a brief refractory period and gradual recovery (with a slight overshoot). **e**, Connectivity and coupling filters from other cells in the population. The black filled ellipse is this cell's RF centre, and blue and red lines show connections from neighbouring OFF and ON cells, respectively (line thickness indicates coupling strength). Below, exponentiated coupling filters show the multiplicative effect on this cell's spike rate after a spike in a neighbouring cell. **f–h**, Analogous plots for an example OFF cell.

model's stimulus filters and nonlinearities (see Supplementary Information), indicating that the difference in performance arises specifically from the coupled model's ability to incorporate the correlation structure. Our results also show that spike history is relevant for decoding (a Poisson model preserves 6% less information than the uncoupled model<sup>22</sup>) and that restricting to a linear decoder further reduces the information that can be recovered from RGC responses.

Decoding analysis can also be used to examine the coding fidelity of specific stimulus features. As a simple illustration, we examined the temporal frequency spectrum of reconstructed stimuli and found that the response correlation structure is most important for decoding those stimulus frequencies (6–20 Hz) that are encoded with highest fidelity (Fig. 4c).

These results demonstrate that the responses of a population of retinal ganglion cells are well described by a generalized linear model, and that correlations in the response can be exploited to recover 20% more visual information than if responses are regarded as independent given the stimulus. In contrast, previous studies have reported this information gain to be less than 10% for pairs of neurons<sup>9,12</sup>. However, pairwise analyses provide little evidence about the importance of correlations across an entire population. Second-order correlations between pairs of neurons could give rise to either much larger (scaling with the number of neurons  $n$ ) or much smaller (falling as  $1/n$ ) gains for a full population (see Supplementary Information). To compare more directly with previous findings,

we performed Bayesian decoding using isolated pairs of neurons from the same population; we found a  $\leq 10\%$  gain in sensory information when correlations were included (see Supplementary Information). This is consistent with previous findings, and shows that the information gain for a complete population is larger than that observed for pairs. We also compared the model to a pairwise maximum-entropy model, which has recently been shown to capture the instantaneous spiking statistics of groups of retinal ganglion cells<sup>14,15</sup>. The coupled model exhibits similar accuracy in capturing these statistics, but has the advantage that it accounts for the temporal correlation structure and stimulus dependence of responses, which are essential for assessing the effect of correlations on sensory coding.

Although it provides an accurate functional description of correlated spike responses, the generalized linear model does not reveal the biophysical mechanisms underlying the statistical dependencies between neurons: coupling does not necessarily imply anatomical connections between cells, but could (for example) reflect dependencies due to shared input noise<sup>1</sup>. The model also lacks several mechanisms known to exist in retinal ganglion cells (for example, contrast gain-control<sup>23</sup>), which may be required for characterizing responses to a wider variety of stimuli. One additional caveat is that Bayesian decoding provides a tool for measuring the sensory information available in the population response, but it does not reveal whether the brain makes use of this information.

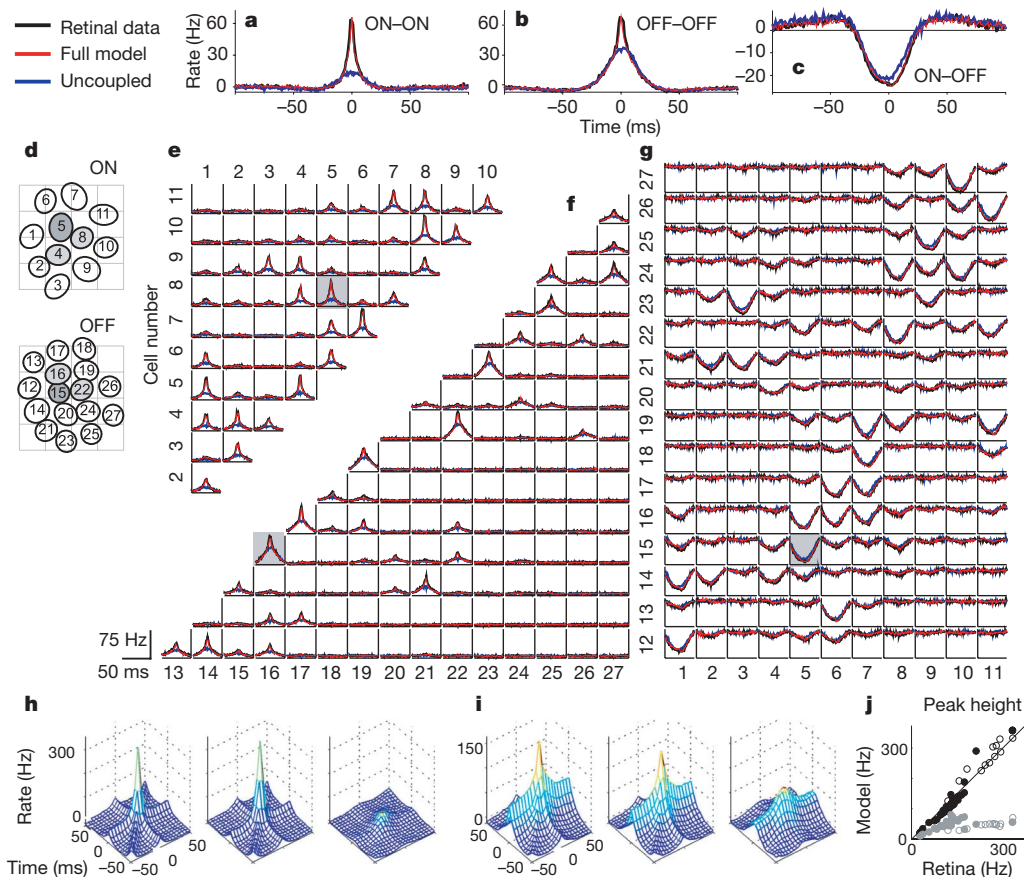


**Figure 2 | Analysis of response correlations.** **a–c**, Example CCFs of retinal responses, and simulated responses of the full and uncoupled models, for two ON cells (**a**), two OFF cells (**b**) and an ON–OFF pair (**c**). The baseline is subtracted so that units are in spikes per s above (or below) the cell's mean rate. **d**, Receptive field mosaic overlaid with arbitrary labels. Dark grey indicates cells shown in Fig. 1; light grey indicates cells used for triple correlations (**h**, **i**). **e**, CCFs between all ON pairs, where the  $i,j$ th plot shows the CCF between cell  $i$  and cell  $j$ . The grey box indicates the CCF plotted in

**a, f, g**, CCFs between all OFF–OFF pairs (**f**) and all ON–OFF pairs (**g**; abscissa height is 30 Hz). **h**, Third-order (triplet) CCF between three adjacent ON cells, showing the instantaneous spike rate of cell 5 as a function of the relative spike time in cells 4 and 8 (left, RGCs; middle, full model; right, uncoupled model). **i**, Analogous triplet CCF for OFF cells 15, 16 and 22. **j**, Comparison of the triplet CCF peak in RGC and model responses (full model, black; uncoupled, grey) for randomly selected triplets of adjacent ON (open) and OFF (filled) cells.

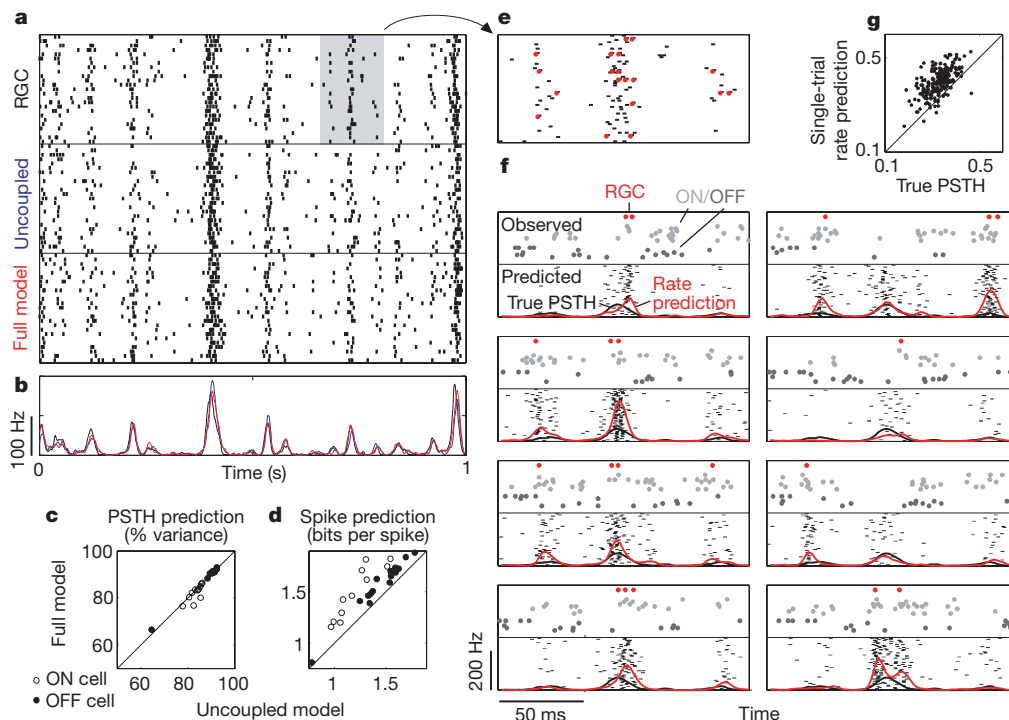


**Figure 3 | Spike-train prediction comparison.** **a**, Raster of responses of an ON RGC to 25 repeats of a novel 1-s stimulus (top), and responses of uncoupled (middle) and full (bottom) models to the same stimulus. **b**, PSTH of the RGC (black), uncoupled (blue) and coupled (red) model; both models account for ~84% of the variance of the true PSTH. **c**, PSTH prediction by full and uncoupled models, showing that coupling confers no advantage in predicting average responses. **d**, Log-likelihood of novel RGC spike responses under full and uncoupled models; the full model provides 8% more information about novel spike trains. **e**, Magnified 150-ms portion of RGC raster and PSTH (grey box in **a**). Red dots highlight RGC spike times on selected individual trials, which are replotted in **f**. **f**, Single-trial spike-train prediction using the coupled model. The top half of each plot shows the

population activity on a single trial: true spike times of the cell (red dots), coupled ON cells (light grey dots) and coupled OFF cells (dark grey dots; each line in the raster shows the spike times of a different cell). The bottom half of each plot shows a raster of 50 predicted responses of the cell in question, using both the stimulus and coupled responses (shown above) to predict spike trains. The red trace shows the single-trial rate prediction (population-conditioned PSTH), compared with true PSTH of the cell (black trace, identical in all plots). **g**, Correlation coefficient of true spike trains with the PSTH (ordinate) and with population-conditioned predictions (abscissa); the full model predicts single-trial responses with higher accuracy than the true PSTH.

Physiological interpretations of the model and mechanisms for neural read-out of sensory information in higher brain areas are thus important directions for future research.

Nevertheless, the generalized linear model offers a concise, computationally tractable description of the population encoding process, and provides the first generative description of the space-time dependencies in stimulus-induced population activity. It allows us to quantify the relative contributions of stimulus, spike history and

network interactions to the encoding and decoding of visual stimuli, and clarifies the relationship between single-cell and population variability. More generally, the model can be used to assess which features of the visual environment are encoded with highest and lowest fidelity, and to determine how the structure of the neural code constrains perceptual capabilities. We expect this framework to extend to other brain areas, and to have an important role in revealing the information processing capabilities of spiking neural populations<sup>4,19,24,25</sup>.

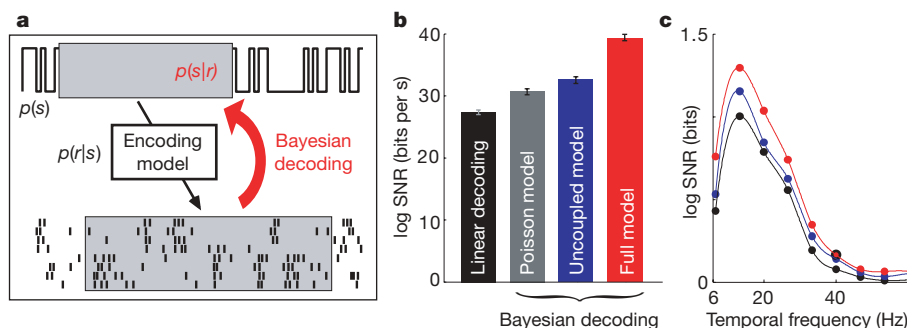


**Figure 4 | Decoding performance comparison.** **a**, Shown is a Bayesian decoding schematic: to estimate an unknown stimulus segment from a set of observed spike times (highlighted in boxes), the stimulus prior distribution  $p(s)$  is multiplied by the model-defined likelihood  $p(r|s)$  to obtain the posterior  $p(s|r)$ . The posterior mean is the Bayes' least-squares stimulus estimate. **b**, Log of the SNR for linear decoding, as well as for Bayesian decoding under the Poisson, uncoupled and full models<sup>6</sup>. The full model

preserves 20% more information than the uncoupled model, which indicates that there is additional sensory information available from the population response when correlations are taken into account. Error bars show 95% confidence intervals based on 2,000 bootstrap resamplings of 3,000 decoded stimulus segments. **c**, Log SNR decomposed as a function of temporal frequency for various decoding methods (Poisson omitted for clarity).



## METHODS SUMMARY

**Data.** Multi-electrode extracellular recordings were obtained *in vitro* from a segment of isolated, peripheral macaque monkey (*Macaca mulatta*) retina, and analysis was restricted to two cell types (ON and OFF parasol)<sup>15,26,27</sup>. A standard spike-sorting procedure, followed by a specialized statistical method for detecting simultaneous spikes, was used to sort spikes (see ref. 28). The retina was stimulated with a photopic, achromatic, optically reduced spatio-temporal binary white noise stimulus refreshing at 120 Hz, with a root-mean-square contrast of 96%.

**Fitting.** Model parameters were fitted to 7 min of spike responses to a non-repeating stimulus. Each cell's parameters consisted of a stimulus filter (parametrized as a rank-2 matrix), a spike-history filter, a set of incoming coupling filters and a constant. Temporal filters were represented in a basis of cosine 'bumps'<sup>22</sup>. Parameters for the uncoupled and Poisson (LNP) models were fitted independently. Parameters were fitted by penalized maximum likelihood<sup>4,5</sup>, with an L1 penalty on the vector length of coupling filters to eliminate unnecessary connections.

**Encoding.** Spike prediction was cross-validated using the log-likelihood of 5 min of novel spiking data (scaled to units of bits per s). Repeat rasters were obtained using 200 presentations of a novel 10-s stimulus. Population-conditional rasters were obtained from the coupled model by sampling the model-defined probability distribution over the neuron's response given the stimulus and surrounding-population activity on a single trial<sup>29</sup>.

**Decoding.** Population responses were decoded using the Bayes' least-squares estimator (posterior mean) to reconstruct 18-sample single-pixel stimulus segments (cross-validation data). Linear decoding was performed using the optimal linear estimator<sup>6</sup>. Decoding performance was quantified using the log signal-to-noise ratio (SNR) of each technique, which gives an estimate of mutual information. Breakdown by temporal frequency was obtained by computing the Fourier power spectra of the stimuli and residuals and then computing log SNR.

**Full Methods** and any associated references are available in the online version of the paper at [www.nature.com/nature](http://www.nature.com/nature).

Received 16 July 2007; accepted 5 June 2008.

Published online 23 July 2008.

1. Mastrorade, D. N. Correlated firing of retinal ganglion cells. *Trends Neurosci.* **12**, 75–80 (1989).
2. Meister, M., Lagnado, L. & Baylor, D. A. Concerted signaling by retinal ganglion cells. *Science* **270**, 1207–1210 (1995).
3. Shadlen, M. & Newsome, W. The variable discharge of cortical neurons: implications for connectivity, computation, and information coding. *J. Neurosci.* **18**, 3870–3896 (1998).
4. Truccolo, W., Eden, U. T., Fellows, M. R., Donoghue, J. P. & Brown, E. N. A point process framework for relating neural spiking activity to spiking history, neural ensemble and extrinsic covariate effects. *J. Neurophysiol.* **93**, 1074–1089 (2004).
5. Paninski, L. Maximum likelihood estimation of cascade point-process neural encoding models. *Network Comp. Neural Syst.* **15**, 243–262 (2004).
6. Warland, D., Reinagel, P. & Meister, M. Decoding visual information from a population of retinal ganglion cells. *J. Neurophysiol.* **78**, 2336–2350 (1997).
7. Dan, Y., Alonso, J. M., Usrey, W. M. & Reid, R. C. Coding of visual information by precisely correlated spikes in the lateral geniculate nucleus. *Nature Neurosci.* **1**, 501–507 (1998).
8. Panzeri, S., Golledge, H., Zheng, F., Tovee, M. P. & Young, M. J. Objective assessment of the functional role of spike train correlations using information measures. *Vis. Cogn.* **8**, 531–547 (2001).
9. Nirenberg, S., Carcieri, S., Jacobs, A. & Latham, P. Retinal ganglion cells act largely as independent encoders. *Nature* **411**, 698–701 (2001).
10. Schneidman, E., Bialek, W. & Berry, M. J. Synergy, redundancy, and independence in population codes. *J. Neurosci.* **21**, 11539–11553 (2003).
11. Nirenberg, S. & Latham, P. E. Decoding neuronal spike trains: how important are correlations? *Proc. Natl Acad. Sci. USA* **100**, 7348–7353 (2003).
12. Averbach, B. & Lee, D. Coding and transmission of information by neural ensembles. *Trends Neurosci.* **27**, 225–230 (2004).
13. Latham, P. & Nirenberg, S. Synergy, redundancy, and independence in population codes, revisited. *J. Neurosci.* **25**, 5195–5206 (2005).
14. Schneidman, E., Berry, M., Segev, R. & Bialek, W. Weak pairwise correlations imply strongly correlated network states in a neural population. *Nature* **440**, 1007–1012 (2006).
15. Shlens, J. *et al.* The structure of multi-neuron firing patterns in primate retina. *J. Neurosci.* **26**, 8254–8266 (2006).
16. Plesser, H. & Gerstner, W. Noise in integrate-and-fire neurons: From stochastic input to escape rates. *Neural Comput.* **12**, 367–384 (2000).
17. Simoncelli, E. P., Paninski, L., Pillow, J. & Schwartz, O. in *The Cognitive Neurosciences* 3rd edn (ed. Gazzaniga, M.) 327–338 (MIT, 2004).
18. Frechette, E. S. *et al.* Fidelity of the ensemble code for visual motion in primate retina. *J. Neurophysiol.* **94**, 119–135 (2005).
19. Okatan, M., Wilson, M. & Brown, E. Analyzing functional connectivity using a network likelihood model of ensemble neural spiking activity. *Neural Comput.* **17**, 1927–1961 (2005).
20. Rigat, F., de Gunst, M. & van Pelt, J. Bayesian modelling and analysis of spatio-temporal neuronal networks. *Bayes. Anal.* **1**, 733–764 (2006).
21. DeVries, S. H. Correlated firing in rabbit retinal ganglion cells. *J. Neurophysiol.* **81**, 908–920 (1999).
22. Pillow, J. W., Paninski, L., Uzzell, V. J., Simoncelli, E. P. & Chichilnisky, E. J. Prediction and decoding of retinal ganglion cell responses with a probabilistic spiking model. *J. Neurosci.* **25**, 11003–11013 (2005).
23. Shapley, R. M. & Victor, J. D. The effect of contrast on the transfer properties of cat retinal ganglion cells. *J. Physiol.* **285**, 275–298 (1978).
24. Harris, K., Csicsvari, J., Hirase, H., Dragoi, G. & Buzsaki, G. Organization of cell assemblies in the hippocampus. *Nature* **424**, 552–556 (2003).
25. Paninski, L., Fellows, M., Shoham, S., Hatsopoulos, N. & Donoghue, J. Superlinear population encoding of dynamic hand trajectory in primary motor cortex. *J. Neurosci.* **24**, 8551–8561 (2004).
26. Litke, A. M. *et al.* What does the eye tell the brain? Development of a system for the large scale recording of retinal output activity. *IEEE Trans. Nucl. Sci.* **51**, 1434–1440 (2004).
27. Watanabe, M. & Rodieck, R. W. Parasol and midget ganglion cells of the primate retina. *J. Comp. Neurol.* **289**, 434–454 (1989).
28. Segev, R., Goodhouse, J., Puchalla, J. & Berry, M. J. Recording spikes from a large fraction of the ganglion cells in a retinal patch. *Nature Neurosci.* **7**, 1155–1162 (2004).
29. Pillow, J. W. & Latham, P. in *Advances in Neural Information Processing Systems 20* (eds Platt, J. C., Koller, D., Singer, Y. & Roweis, S.) 1161–1168 (MIT, 2008).

**Supplementary Information** is linked to the online version of the paper at [www.nature.com/nature](http://www.nature.com/nature).

**Acknowledgements** We thank M. Bethge, C. Brody, D. Butts, P. Latham, M. Lengyel, S. Nirenberg and R. Sussman for comments and discussions; G. Field, M. Greschner, J. Gauthier and C. Hulse for experimental assistance; M. I. Grivich, D. Petrusca, W. Dabrowski, A. Grillo, P. Grybos, P. Hottowy and S. Kachiguine for technical development; H. Fox, M. Taffe, E. Callaway and K. Osborn for providing access to retinas; and S. Barry for machining. Funding was provided a Royal Society USA/Canada Research Fellowship (J.W.P.); NSF IGERT DGE-03345 (J.S.); NEI grant EY018003 (E.J.C., L.P. and E.P.S.); Gatsby Foundation Pilot Grant (L.P.); Burroughs Wellcome Fund Career Award at the Scientific Interface (A.S.); US National Science Foundation grant PHY-0417175 (A.M.L.); McKnight Foundation (A.M.L. and E.J.C.); and HHMI (J.W.P., L.P. and E.P.S.).

**Author Information** Reprints and permissions information is available at [www.nature.com/reprints](http://www.nature.com/reprints). Correspondence and requests for materials should be addressed to J.W.P. ([pillow@gatsby.ucl.ac.uk](mailto:pillow@gatsby.ucl.ac.uk)).

## METHODS

**Recording.** Multi-electrode extracellular recordings were obtained *in vitro* from a segment of isolated, peripheral macaque monkey retina, using preparation and recording methods described previously<sup>15,26</sup>. Analysis was restricted to two physiologically defined classes of cells; on the basis of light response properties and density, these were identified as ON and OFF parasol cells<sup>27</sup>. The cells shown were recorded in a square region of retina covered by 76 electrodes. A standard clustering-based spike-sorting procedure (see refs 15, 26) was used to estimate the number of units, and least-squares regression of the estimated spike times against multi-electrode voltage signal was used to estimate multi-electrode spike waveforms for each unit. Although this approach correctly and efficiently identifies isolated spikes, when two cells fire within a 1–2-ms window, the clustering approach can fail to identify the presence of both spikes. We solved this problem by using estimates of the elementary waveforms to detect the superposition of spikes. We performed maximum *a posteriori* estimation under the model that the multi-electrode voltage signal was the linear superposition of Gaussian white noise and the spike trains convolved with their associated spike waveforms, with a sparse (exponential) prior distribution on the spike trains. This corresponds to a tractable quadratic optimization problem under linear inequality constraints, which can be solved efficiently using existing methods. The real-valued solution vector was then binarized by greedily inserting spikes whenever the reduction in mean-squared error between predicted and actual voltage exceeded a threshold<sup>28</sup>. This procedure correctly identified simultaneous spikes in simulated data sets and corrected obvious cross-correlation artefacts appearing in real data sorted with standard clustering techniques.

**Stimuli.** The retina was stimulated with a photopic, achromatic image of a cathode ray tube display, refreshing at 120 Hz. The stimulus was a spatio-temporal pseudo-random binary sequence, where the intensity of each pixel was drawn independently from one of two values on each frame. The stimulus pixel size was  $120 \times 120 \mu\text{m}$  on the retina, and contrast (standard deviation divided by mean) was 96%.

**Fitting.** Model parameters were fitted by maximizing likelihood<sup>5</sup> using 7 min of spiking data recorded during presentation of a non-repeating stimulus. The parameters for each cell consisted of a stimulus filter  $\mathbf{k}$ , a spike-history filter  $\mathbf{h}$ , a set of incoming coupling filters  $\{\mathbf{l}_i\}$  and a constant (specifying the log of the baseline firing rate)  $\mu$ . The filter  $\mathbf{k}$  was a 750-dimensional vector ( $5 \times 5$  spatial pixels  $\times$  30 time bins), parametrized using a lower-dimensional representation as a rank-2 matrix:  $k(x, y, \tau) = k_{s,1}(x, y)k_{t,1}(\tau) + k_{s,2}(x, y)k_{t,2}(\tau)$ , with  $k_{s,i}(x, y)$  denoting a spatial filter (25 parameters) and  $k_{t,i}(\tau)$  a temporal filter (10 parameters), giving  $2 \times 35 = 70$  parameters. A rank-3 representation did not improve performance. These filters closely resembled a time-varying difference-of-Gaussians<sup>30</sup>; spatial filters were well-approximated (in a least-squares sense) by Gaussians, which were used to plot spatial ellipses shown in Fig. 1 and to summarize receptive field properties (Supplementary Figs 2 and 3). Gaussians fit to receptive field centres and surrounds had average standard deviations of 0.25 pixels and 0.7 pixels (1.0 pixels for the uncoupled model), respectively. Temporal filters  $\mathbf{h}$  and  $\{\mathbf{l}_i\}$  and the temporal components of  $\mathbf{k}$  were represented using a basis of raised cosine ‘bumps’ of the form  $\mathbf{b}_j(t) = (1/2)\cos(a\log[t+c] - \phi_j) + (1/2)$  for  $t$  such that  $a\log(t+c) \in [\phi_j - \pi, \phi_j + \pi]$  and 0 elsewhere, with constants  $a$  and  $c$  set by hand to match the structure observed in auto- and cross-correlation functions, and  $\pi/2$  spacing between the  $\phi_j$  (see Supplementary Information). This basis allows for the representation of fine temporal structure near the time of a spike and coarser/smoother dependency at later times (see ref. 22). The  $\mathbf{h}$  filter was represented with ten such basis vectors, and the  $\mathbf{l}_i$  coupling filters were represented with four. The ‘uncoupled model’ was fitted independently without coupling filters  $\{\mathbf{l}_i\}$ , and the inhomogeneous Poisson model (Fig. 4) was fitted without  $\{\mathbf{l}_i\}$  or  $\mathbf{h}$ .

Conditional intensity (spike rate) is given by  $\lambda(t) = \exp(\mathbf{k} \cdot \mathbf{x} + \mathbf{h} \cdot \mathbf{y} + (\sum_i \mathbf{l}_i \cdot \mathbf{y}_i) + \mu)$ , where  $\mathbf{x}$  is the stimulus,  $\mathbf{y}$  the cell’s own spike-train history,  $\mu$  is the cell’s baseline log-firing rate, and  $\{\mathbf{y}_i\}$  the spike-train histories of other cells at time  $t$ . The population log-likelihood is the sum over single-cell

log-likelihoods, each given by  $L = \sum \log \lambda(t_{sp}) - \lambda(t)dt$ , where  $t_{sp}$  denotes the set of spike times and the integral is taken over the length of the experiment<sup>4,5</sup>. We added a penalty of the form  $-\alpha \int |\sum_i \mathbf{l}_i(t)|^{1/2} dt$  to eliminate unnecessary coupling filters (using a constrained Newton–Raphson algorithm to maximize the penalized log-likelihood), which regularizes and prevents overfitting. The regularization parameter  $\alpha$  was selected by means of cross-validation on a novel 5-min data set, but results were robust with respect to both  $\alpha$  and the choice of basis. (This reduced the number of coupling filters from 702 to 243 and recovered a roughly pairwise-adjacent structure; see Supplementary Information.)

**Correlations.** Spike responses of full and uncoupled models were simulated with the same 20-min stimulus (144,000 samples) presented experimentally. Pairwise cross-correlations were computed in 1-ms bins, according to  $C(\tau) = [\langle y_1(t)y_2(t+\tau) \rangle - \langle y_1(t) \rangle \langle y_2(t) \rangle] / (\langle y_2(t) \rangle dt)$ , where  $y_1(t)$  denotes the spike response of the first neuron in bins of width  $dt$ , and  $\langle \cdot \rangle$  denotes averaging over  $t$ . Triplet correlations were computed in 5-ms bins according to  $C(\tau_1, \tau_2) = [\langle y_1(t)y_2(t+\tau_1)y_3(t+\tau_2) \rangle - \langle y_1(t) \rangle \langle y_2(t) \rangle \langle y_3(t) \rangle] / (\langle y_2(t) \rangle \langle y_3(t) \rangle dt)$ .

**Encoding.** Spike-train prediction was validated using the log-likelihood of novel spike trains under both models, computed on 5 min of data not used for fitting or setting  $\alpha$ . The difference of log-likelihood under the model and log-likelihood under a homogeneous Poisson process,  $\sum \log \lambda(t_{sp}) - \int \lambda(t)dt$  (where  $\bar{\lambda} = n_{sp}/T$  is the mean spike rate), divided by  $n_{sp}$ , gives prediction accuracy in bits per spike for each cell<sup>25</sup>. Repeat rasters were obtained using 200 presentations of a novel 10-s stimulus, and the time-varying average response (PSTH) was computed in 1-ms bins, smoothed with a Gaussian kernel of width  $\sigma = 2$  ms. Conditional rasters were obtained from the coupled model by holding the responses of all but one neuron fixed, and sampling from the model-induced probability distribution on the remaining neuron’s response. Samples were obtained by the Metropolis–Hastings algorithm, with spike ‘proposals’ drawn from a point process model as described in ref. 29. We kept only every 100th output sample of the algorithm to ensure independent samples.

**Decoding.** We decoded the population response using the Bayes’ least-squares estimator, computed under each model (fully coupled, uncoupled with spike-history terms, and inhomogeneous Poisson) using 6,000 different 18-sample single-pixel stimulus segments (validation data that were not used for fitting). Each stimulus  $\mathbf{x}_i$  (an 18-dimensional binary vector, given by the time series of light intensities for a centrally located stimulus pixel) was decoded by first extracting  $\mathbf{y}_i$ , the multi-neuronal spike response portion that was causally influenced by this stimulus. For each model, and for every one of the  $2^{18}$  possible binary  $\mathbf{x}_j$ , we then computed  $p_j = p(\mathbf{y}_i | \mathbf{x}_j)$ , the likelihood of the observed population response given that it was generated by stimulus  $\mathbf{x}_j$ . By Bayes’ rule, the posterior is  $p(\mathbf{x}_j | \mathbf{y}_i) \propto p(\mathbf{y}_i | \mathbf{x}_j)p(\mathbf{x}_j)$ , and the prior  $p(\mathbf{x}_j)$  here is constant across binary stimuli. Thus, the posterior is proportional to  $p_j$ , and the Bayes’ least-squares estimate is given by  $\hat{\mathbf{x}}_i = (\sum p_j \mathbf{x}_j) / (\sum p_j)$ . We also performed decoding on longer (30-sample) stimulus segments, where exhaustive evaluation of these sums is no longer tractable: in this case we used Gibbs sampling from  $p(\mathbf{x}_j | \mathbf{y}_i)$  to approximately evaluate the sum. The results obtained using both methods were similar.

Linear decoding was performed using the optimal linear estimator<sup>6</sup>, with the same training data as for model fitting. Decoding performance was quantified using the log SNR of each technique:  $\log \left( \frac{|\langle \mathbf{x}_i \mathbf{x}_i^T \rangle|}{\langle \mathbf{r}_i \mathbf{r}_i^T \rangle} \right)$ , where  $\mathbf{r}_i = \hat{\mathbf{x}}_i - \mathbf{x}_i$  denotes the residual error for decoding stimulus vector  $\mathbf{x}_i$ , and  $\langle \cdot \rangle$  denotes averaging over  $i$  followed by matrix determinant. Breakdown by temporal frequency was obtained by computing the Fourier power spectra of the stimuli  $\hat{\mathbf{x}}_i(\omega)^2$  and residuals  $\hat{\mathbf{r}}_i(\omega)^2$ , and computing log SNR according to  $\log(\langle \hat{\mathbf{x}}_i(\omega)^2 \rangle / \langle \hat{\mathbf{r}}_i(\omega)^2 \rangle)$ . Integrating this log SNR across frequency,  $(1/2) \int \log \text{SNR}(\omega) d\omega$ , gives a commonly used estimate of the mutual information between the stimulus and the spike-train response<sup>6</sup>, which is equivalent to the quantity shown in Fig. 4b.

30. Meister, M. & Berry, M. J. The neural code of the retina. *Neuron* 22, 435–450 (1999).

## SUPPLEMENTARY INFORMATION

## Spatio-temporal correlations and visual signaling in a complete neuronal population

Jonathan W. Pillow<sup>1</sup>, Jonathon Shlens<sup>2</sup>, Liam Paninski<sup>3</sup>,  
Alexander Sher<sup>4</sup>, Alan M. Litke<sup>4</sup>, E. J. Chichilnisky<sup>2</sup>, Eero P. Simoncelli<sup>5</sup>

<sup>1</sup> Gatsby Computational Neuroscience Unit, UCL

<sup>2</sup> The Salk Institute, La Jolla, California

<sup>3</sup> Department of Statistics and Center for Theoretical Neuroscience, Columbia University

<sup>4</sup> Santa Cruz Institute for Particle Physics, University of California, Santa Cruz

<sup>5</sup> Howard Hughes Medical Institute, Center for Neural Science,  
and Courant Institute of Mathematical Sciences, New York University

Correspondence should be addressed to J.W.P. (pillow@gatsby.ucl.ac.uk)

May 23, 2008

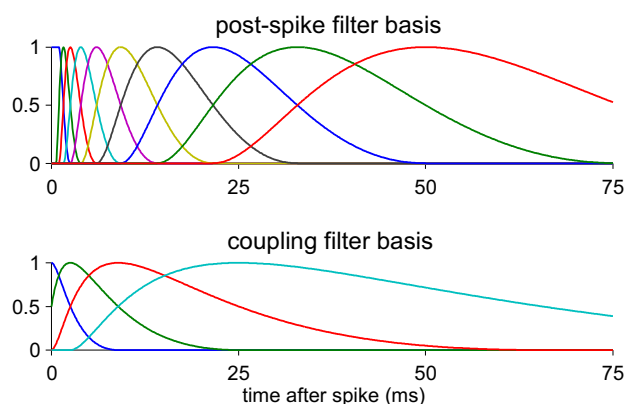
## Supplementary Materials

To provide more insight into the generalized linear model, we present several figures illustrating details of the model components and their contributions to model response properties. We also discuss several control analyses addressing whether the difference in performance of the full and uncoupled models can be attributed primarily to their difference in capturing the response correlation structure. Finally, we provide connections to several previous results on correlated spiking activity in neural populations, specifically maximum-entropy analyses [1, 2] and pairwise measurements of coding efficiency [3].

### Analysis of Model Components

Figure S1 shows the linear bases used to parametrize post-spike filters and coupling filters, respectively. These bases provide a low-dimensional parametrization of the waveforms, allowing for fine temporal

structure near the time of a spike and coarse temporal structure at longer delays. The raised cosine form for these vectors means they sum to a constant and are free of temporal aliasing.



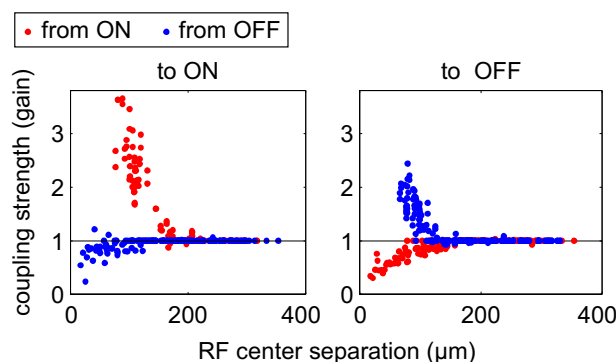
**Figure S1:** Bases used for representing spike-history and coupling filters. Basis vectors have the form of raised cosine “bumps”, so they sum to a constant, and have log-scaling of the time axis, so they can represent fine structure near the time of a spike and coarser structure on longer timescales using a restricted number of parameters (see Methods). Filters were fit as a weighted linear combination of the basis vectors. **Above:** 10-dimensional basis for post-spike filters. **Below:** 4-dimensional basis for coupling filters.

Figure S2 shows that coupling strength falls off strongly with the distance between receptive field (RF) centers, illustrating the fact that coupling effects are primarily restricted to neighboring cells (cf. [2]). Coupling between ON cells is on average much stronger and extends over larger distances than between OFF cells.

Comparison of the fitted parameters obtained for the full and uncoupled models provides insight into the manner in which correlations affect stimulus processing in the retina. Specifically, the spatial extent of the receptive field “surround” mechanism is larger for the uncoupled model than for the full model (fig. S3). This indicates that, when population activity is taken into account, each cell integrates light from an effectively smaller region. In other words, the effect of stimuli far out in the surround can be more parsimoniously explained in terms of population spiking activity. Classical estimates of receptive fields, such as the spike-triggered average, do not resolve such effects. The functional consequence of this change in receptive field structure (fig. S3c) is to make stimulus filters more orthogonal to one another, meaning that stimulus drive is more independent across neurons under the full model.

To examine the relative magnitude of the inputs provided by stimulus and coupling-related model components, we show the net linear input to an example ON cell from the stimulus filter and from coupling filters from ON cell and to OFF cell activity (fig. S4). The sum of these inputs (including





**Figure S2:** Connectivity summary, showing strength of coupling between cells vs. the distance between their RF centers. Coupling strength is quantified as the exponentiated amplitude of the largest absolute peak of the filter  $\exp(f(x_{peak}))$ , where  $x_{peak} = \arg \max_x |f(x)|$ . **Left:** strength of incoming coupling filters to ON cells. **Right:** coupling filters into OFF cells. Points on the line  $y=1$  indicate an absence of coupling (i.e., filters eliminated by the sparse prior). Absence of ON-ON and OFF-OFF points within the range 0–70  $\mu\text{m}$  reflects the minimum spacing between cells within a single mosaic.

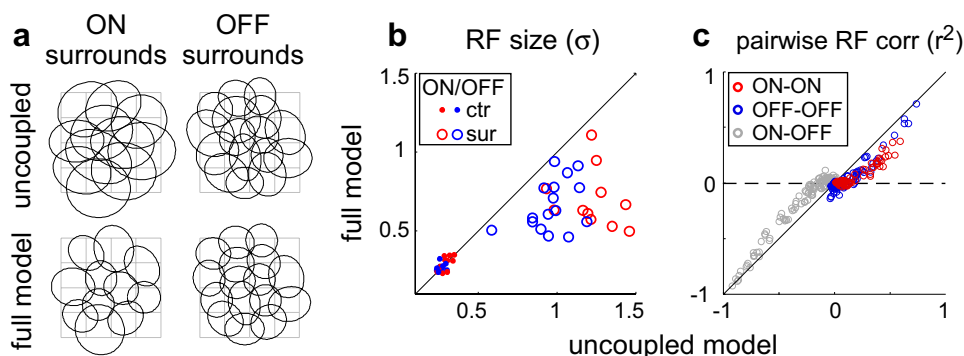


**Figure S3:** Receptive field changes induced by coupling. **a**, Ellipses show 1 SD contours of a Gaussian fit to the surround mechanism for each cell, for uncoupled (above) and full models (below). **b**, Scatter-plot of RF center and surround sizes; each point represents the estimated RF diameter of a single cell under full and uncoupled models. Surround width is reduced by roughly 70% in the coupled model, while the center width is roughly constant. **c**, Correlation coefficients between all pairs of RFs, under uncoupled (x-axis) and full models (y-axis), showing RFs to be more orthogonal (i.e., closer to zero-correlation) under the full model (cf. [4]).

post-spike filter output) can be loosely interpreted as membrane potential in a “soft-threshold integrate-and-fire” model: the exponential nonlinearity forms a soft threshold whereby the probability of spiking increases as a smooth function of membrane depolarization [5]. The relative importance of network- and stimulus-induced inputs to each cell can be roughly quantified by the amplitude of the fluctuations they induce in the membrane voltage. Across the population, the standard deviation of the total network-induced input is approximately 1/2 the standard deviation of the stimulus-induced input in ON cells, and 1/3 in OFF cells.

For each cell, the model converts linear input into an instantaneous spike rate by means of an expo-

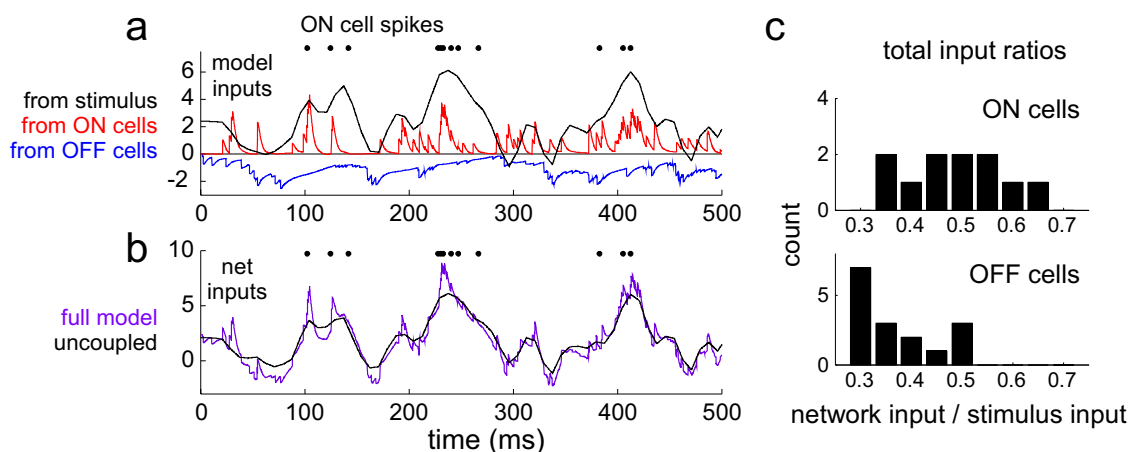


**Figure S4:** Relative contribution of stimulus and coupling dependent inputs to an example ON cell. **a**, Net linear input from the stimulus, ON cells, and OFF cells during a 500ms stimulus segment on a single trial, with true spike times of the ON cell shown above (black dots). Traces show the output of the stimulus filter (black), and the summed outputs of coupling filters from ON cells (red) and from OFF cells (blue). **b**, Summing the three traces above gives the net external input to the cell (purple trace), plotted alongside the stimulus-dependent input to this cell under the uncoupled model (its only external input). Exponentiating the total input (which also includes input from the post-spike filter, omitted here for visual clarity) gives the instantaneous spike rate of the model. **c**, Histogram showing the relative magnitude of stimulus and population-induced inputs to each cell under the full model. *x*-axis is the ratio of the standard deviation of each of these inputs (where population input is the sum of ON and OFF inputs). Population-induced input tends to be approximately half as strong as stimulus-induced input in ON cells (above), and about a third as strong in OFF cells (below).

nential nonlinearity. To assess the adequacy of this assumption, we compare an exponential function with a direct “reconstruction” estimate of the nonlinearity, computed using the raw distribution of filter outputs and the observed spike responses (fig. S5) [6]. These reconstructions look reasonably exponential for both uncoupled and full-model parameter settings, though slightly better for ON than OFF cells. For comparison, we also performed a complete re-fitting of the model parameters using output nonlinearities given by a half-wave rectified linear function and by  $\log(1 + \exp(x))$ , which grows linearly for large  $x$  and decays like  $e^x$  for negative values. These models gave much lower likelihoods for the observed data and exhibited poorer cross-validation performance.

Finally, we re-fit both full and coupled models using a flexible nonlinearity, parametrized as a cubic spline with 8 piecewise polynomial segments. This addition conferred a slight improvement in cross-validation performance (see fig. S7), and it did not elicit a noticeable change in the fitted filters. We

return to this model under Control Analyses, below.

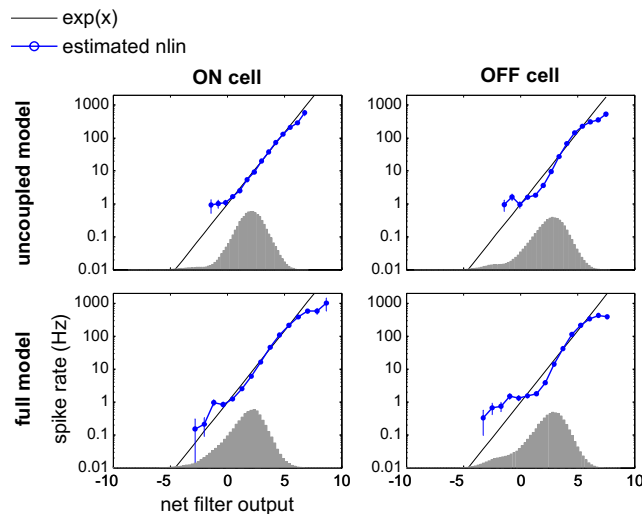


**Figure S5:** Histogram-based estimates of the nonlinearity transforming linear input to instantaneous spike rate (blue traces), for an example ON (left) and OFF (right) cell, under uncoupled and full models (above and below, respectively) [6]. The gray histograms show the distribution over the net linear input (i.e., the sum of all filter outputs) across time. The nonlinearity represents the probability of observing a spike for each bin in this histogram (with error bars showing  $\pm 1$  SEM, computed by regarding the spike count in each bin as a binomial random variable). An exponential function (black), the assumed nonlinearity for both models, provides a reasonable approximation to these functions.

## Control Analyses

Although they have the same functional form, one might wonder whether the difference in performance of the full and uncoupled models arises from some functional differences other than the full model's ability to incorporate statistical dependencies between neurons. The text of the main article presents several pieces of evidence that the difference is primarily related to correlations. Firstly, the full and uncoupled models predict the PSTH with roughly equal accuracy in all cells, indicating that the models have the same *average* stimulus-response properties. That is, the coupled model does not describe the nonlinear transformation from stimuli to spikes more accurately, once correlations have been averaged out. Secondly, the fact that single-trial predictions correlate more highly with spike trains than the cell's true PSTH (as shown in fig. 3) demonstrates an improvement that *must* be due to correlations: any model that ignores correlations gives the same prediction on every repeat of the stimulus, and therefore cannot do better than the PSTH itself. Thus, capturing the correlation structure clearly play an important role in the coupled model's improved performance.

Nevertheless, we performed several control analyses to determine whether differences in the nonlinear

behavior of the full and uncoupled models might underlie some of our findings. First, we investigated the significance of the difference in model architecture by fitting the parameters of the coupled model to a set of artificial “shuffled data”; we refer to this as the “shuffle-trained model” (fig. S6). This model had the same connectivity and the same number of parameters as the full model, and therefore the same space of possible nonlinear input-output mappings. Shuffled data were generated by using each cell’s true spike times in conjunction with simulated spikes from neighboring neurons, elicited by a presentation of the same stimulus to the coupled model.<sup>1</sup> These training data therefore preserved the stimulus dependence of the population response but removed its noise correlation structure. Figure S6 shows the coupling filters obtained for an example ON and OFF cell, compared to those estimated for the full model. Unsurprisingly, the shuffle-trained model exhibited similar PSTH prediction to the full and uncoupled models. It exhibited a negligible improvement in predicting spike times (fig. S6, right), and a  $< 1\%$  increase in Bayesian decoding performance (not shown), over the uncoupled model. Therefore, without access to the correlation structure present in simultaneous activity, the full-model architecture behaves like the independent model, and is unable to extract more information from the population responses.

A second group of control analyses was performed using versions of the coupled and uncoupled models with more complicated nonlinear properties (fig. S7). If the full model’s advantage over the uncoupled model were due to richer stimulus-processing capabilities, rather than its ability to capture correlations, one would expect to see the advantage disappear once both models had access to a sufficiently rich class of nonlinearities. We therefore fit the data using several more-complicated “control models”, which included:

- a point process model with a flexible (instead of exponential) nonlinearity for each cell, parametrized

---

<sup>1</sup>We were forced to use simulated data for the shuffled spike-times of neighboring cells due to the fact that we did not have multiple repeats of a long-duration stimulus. We also simulated a full set of simultaneous data from the model to ensure that fitting the full model to this data returned a consistent estimate of the full model parameters. Thus, any stimulus-related features that are capturable by the model were accurately reproduced by this shuffling procedure.



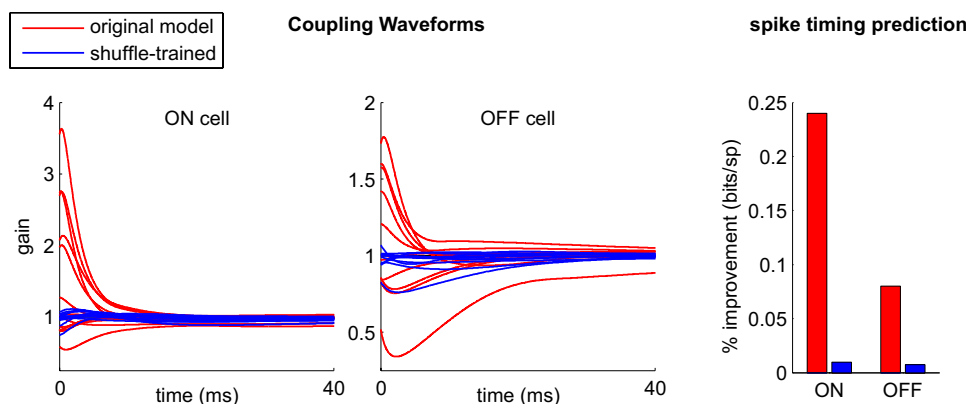


**Figure S6:** Control analysis #1: coupled model trained using shuffled spike data. The coupled model (assuming the same connectivity as the original coupled model) was fit to artificial “shuffled” data, where the stimulus dependence of the spikes used for fitting was intact, but the correlation structure was removed by shuffling. **Left:** coupling waveforms (blue) obtained for an ON and OFF cell fit to shuffled data, compared with the original waveforms fit to the true (simultaneously recorded) data (red). **Right:** improvement in spike timing prediction of the original full and shuffle-trained models over the uncoupled model.

using cubic splines

- a stochastic, leaky integrate-and-fire model with post-spike current ([7], and compared in [8])
- a point process model with multiple stimulus filters (excitatory and suppressive), giving each cell sensitivity to multiple dimensions of the stimulus space (cf. [9]).

In the third model, the conditional intensity depended on the squared outputs of additional excitatory and suppressive filters, and was given by  $\lambda = \lambda_0 \left( \prod_e (1 + (k_e \cdot x)^2) \right) / \left( \prod_i (1 + (k_i \cdot x)^2) \right)$ , where  $\lambda_0$  is the conditional intensity formulated in the original model,  $x$  is the stimulus and  $\{k_e\}$  and  $\{k_s\}$  are stimulus filters providing quadratic excitatory and suppressive input, respectively. We used two excitatory and two suppressive filters, and fit all parameters (including those governing  $\lambda_0$ ) via gradient ascent of the likelihood function. Two versions of each of these control models were fit: one uncoupled, with each cell conditionally independent of the others, and a second with coupling, allowing the model to capture joint dependencies in the response.

For all three control models (fig. S7), the effects of incorporating coupling between cells were directly analogous to the effects in the original model: PSTH prediction was equally accurate with and without

coupling (left panel), while spike-timing prediction (middle) and decoding performance (right) exhibited significant improvements under coupling. Most importantly, the magnitude of the increase in encoding and decoding performance due to coupling was relatively constant across models (i.e., 20% more stimulus information preserved when the population response is decoded under a coupled model). This suggests that the nonlinear stimulus-response properties and response correlation structure make relatively independent contributions to the model's performance. Moreover, these results show that even relatively complicated nonlinear models that ignore correlations do not exceed the performance of the (original) full model. Although not shown here, cross-correlations exhibited by these coupled and uncoupled models are indistinguishable from those of the original full and uncoupled models, indicating that changes in nonlinear stimulus processing do not enhance prediction of the response correlation structure.

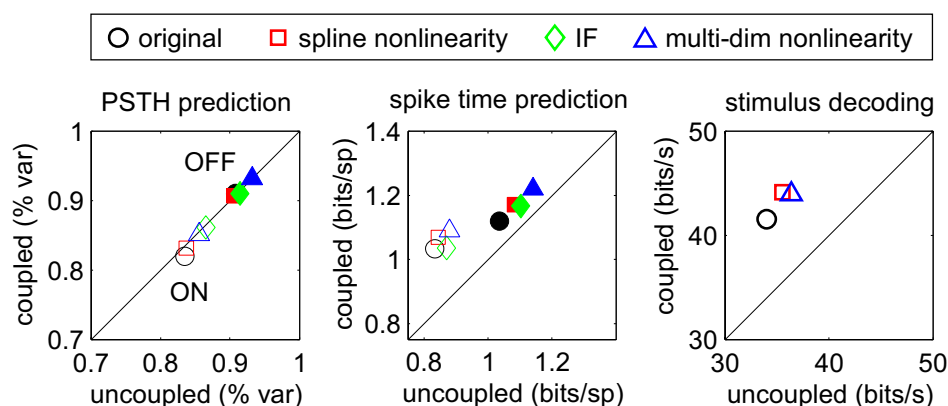


**Figure S7:** Control analysis #2: comparison of coupled and uncoupled models with more complex nonlinear stimulus processing. Models included: (1) a point process model with a flexible nonlinearity, parametrized using cubic splines (red squares); (2) a stochastic, leaky integrate-and-fire model with post-spike aftercurrent [7]; and (3) a point process model with additional excitatory and suppressive stimulus kernels, allowing multi-dimensional dependence on the stimulus. **Left:** Average percent of the PSTH variance accounted for by coupled and uncoupled variants of each model (open symbols = average over ON cells; filled = average over OFF cells). Prediction improves moderately for the more complicated models, but coupled and uncoupled models exhibit no significant difference. **Middle:** Spike-timing prediction (log-likelihood), showing that coupling provides a similar improvement in single-trial spike prediction across models. **Right:** Bayesian decoding of the population response (stimulus reconstruction) improves slightly for more complex models, but the  $\approx 20\%$  improvement conferred by incorporating the response correlation structure is preserved across models (IF model not used due to the computational cost of decoding analysis).

## Comparison to maximum-entropy model predictions

Recent work has suggested that the statistics of retinal ganglion cell population responses, both in the presence and absence of stimulation, are well described by a second-order maximum-entropy (or “max-ent”) model, which describes the maximum-entropy distribution over binary random variables with fixed mean and covariance [1, 2]. To compare our results with these findings, we fit the second-order max-ent model to the simultaneous responses of a population of seven cells and examined the observed and predicted frequencies of 7-digit binary words, indicating which cells spiked in a 10 ms window (for each cell: 0 = ‘no spikes’; 1 = ‘one or more spikes’). We compared RGC word frequencies collected during 8 minutes of stimulation with those emitted by the (simulated) max-ent model and coupled/uncoupled generalized linear point process models (fig. S8). The max-ent and coupled point-process models match the observed frequencies with approximately equal accuracy, while the uncoupled-model prediction is noticeably less inaccurate. The coupled model is therefore consistent with predictions of the second-order max-ent model.

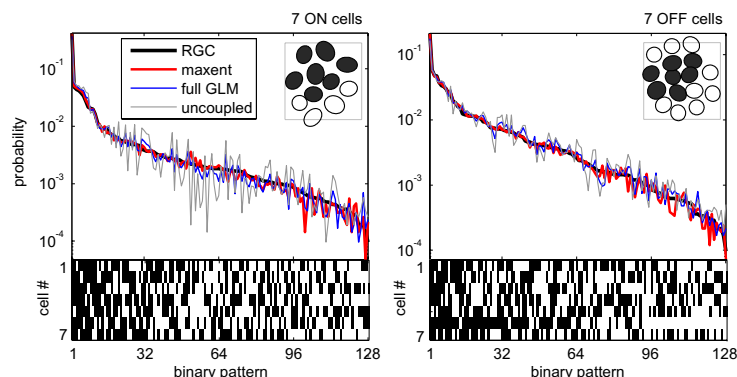


**Figure S8:** Comparison of 7-neuron binary word frequencies with the predictions of a 2nd-order maximum-entropy model [1, 2]. **Left:** Distribution over binary words, computed using simultaneous responses of 7 ON cells (shown inset) in 10 ms bins. Binary words (shown along  $x$  axis) have been sorted by their observed frequency in the actual RGC population response (black trace), and are compared with observed word frequencies from the maximum-entropy (red), coupled (blue) and uncoupled model (gray). **Right:** Analogous plots for a collection of 7 OFF cells. In both cases, the coupled model provides similar accuracy to the max-ent model in predicting word frequencies of RGC population, while the uncoupled model performs substantially less accurately.

However, the generalized linear model makes an important advance over the maximum-entropy model

by incorporating both stimulus dependence and the full time-course of response correlations. Stimulus dependence is especially important, because it is essential for determining whether correlations affect the stimulus-coding properties of the neural population. The max-ent model used here provides a description of the marginal distribution over responses,  $P(\mathbf{r})$ , while the point-process models describes the *conditional* response distribution,  $P(\mathbf{r}|\text{stim})$ ; only the latter distribution captures the relationship between correlations and stimulus encoding.

More generally, the fact that  $P(\mathbf{r})$  can be well described by a second-order maximum entropy model does not imply the same for  $P(\mathbf{r}|\text{stim})$ . We can illustrate this with a simple example: consider 3 neurons encoding 2 discrete stimuli ('A' and 'B') according to the following rule: if A is presented, an odd number of neurons spike, with each possible spike pattern (100, 010, 001, 111) occurring with equal probability; if stimulus B is presented, an even number of neurons spike, again with all possible patterns (000, 011, 101, 110) equally likely. A second-order max-ent model cannot represent the conditional distributions  $P(\mathbf{r}|A)$  and  $P(\mathbf{r}|B)$ , because third-order correlations are essential to this encoding rule—at least one neuron must have access to both its neighbors' responses when deciding whether or not to spike. However, if A and B occur equally often, then all 8 spike patterns occur with equal probability, so the marginal distribution  $P(\mathbf{r})$  is independent, and therefore consistent with a first-order maximum entropy description.

When comparing the second-order maximum-entropy model and the generalized linear point-process model, it is also worth noting that, although both models capture statistical dependencies using pairwise interactions between neurons, responses of the point process model are not necessarily maximum-entropy for any set of constraints on the moments of the response distribution (e.g., 2'nd order correlations). This means that the point-process model does not offer a breakdown of the total entropy by order (i.e., 1st, 2nd, 3rd-order effects), but it might in principle capture higher-order correlations that differ from a second-order maximum entropy prediction.



## Connection to pairwise analyses and Poisson spiking model

Previous work on the importance of correlations in neural coding has focused primarily on pairs of neurons, due in part to the large amounts of data needed for information-theoretic (i.e., model-free) analyses of joint coding [3]. To provide a more direct link to these studies, we repeated the decoding analysis shown in fig. 4 using isolated pairs of neurons. Consistent with earlier findings, we observed that preserving the response correlation structure between pairs provides a  $\leq 10\%$  increase in information. Our results therefore indicate that the full set of spatio-temporal correlations in a neural population account for more information than is observed for isolated pairs.

Analysis of a full population is critical because pairwise analyses can provide little evidence about the importance of correlations across an entire population. Pairwise measurements are blind to third and higher-order response statistics, meaning there is no limit to the information that could be encoded using higher-order features of the population response. Moreover, second-order pairwise correlations can have radically different influences on the information content of the full population (fig. S9). For an idealized example, consider a population of  $n$  neurons, where each neuron contributes  $I_0$  bits independently, and the correlations between any two neurons contribute  $0.2I_0$  bits, so that for any two isolated neurons, the percent increase in information due to the correlations is  $(0.2I_0)/(2I_0) \times 100 = 10\%$ . Now if correlations between any pair of neurons contribute the same information as the correlations between any other pair of neurons (i.e., complete dependence of the pairwise correlations), then the increase due to correlations for the full population is  $(0.2I_0)/(nI_0) \times 100 = (20/n)\%$ , giving a 0.7% increase for our population of 27 cells. On the other hand, if each set of pairwise correlations contributes independent information, the increase due to correlations for the full population is  $\binom{n}{2}0.2I_0/(nI_0) \times 100 = 10(n-1)\%$ , giving a 260% increase for our population (fig. S9). The range of values consistent with pairwise measurements is thus extremely large, and it can increase or decrease with the number of neurons. Determining the importance of correlated spiking across a full population therefore goes significantly beyond the implications of pairwise analyses.

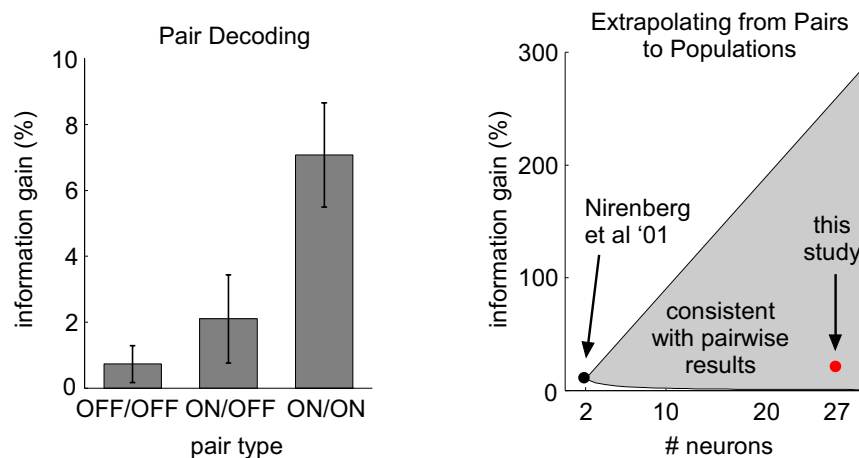


**Figure S9:** Analysis of pairwise decoding. **Left:** To connect with previous literature [3], we performed the same decoding analysis shown in figure 4 using only two neurons at a time. Each bar represents the mean ( $\pm 1$ SD) percent increase in information for decoding under the coupled model vs. under the independent model, for five OFF pairs, five ON-OFF pairs, and five ON-ON pairs. Consistent with earlier findings, incorporating the correlation structure leads to a  $\leq 10\%$  increase in stimulus information. **Right:** Pairwise results alone reveal very little about the importance of correlations in a full population. If including the correlations between two neurons elicits a 10% increase in information (black dot), the 2nd-order correlations in a population of  $n$  neurons can elicit an increase between  $20/n\%$  and  $10(n-1)\%$  (gray region). Our results (red dot) pinpoint the value within this range for a modest-sized population.

Lastly, to connect with one of the standard models in the literature, we compared the encoding performance of the generalized linear point-process model with the classic linear-nonlinear-Poisson (LNP) model [10], which lacks both spike-history dependence and coupling between cells (fig. S10). The LNP model predicts both the PSTH (left) and the timing of spikes (right) less accurately than either the full or the uncoupled model, though it still provides more accurate Bayesian stimulus decoding than an optimal linear decoder (fig. 4).

## References

- [1] E. Schneidman, M. Berry, R. Segev, and W. Bialek. Weak pairwise correlations imply strongly correlated network states in a neural population. *Nature*, 440:1007–1012, 2006.
- [2] J. Shlens, G. Field, J. Gauthier, M. Grivich, D. Petrusca, A. Sher, Litke A. M., and E. J. Chichilnisky. The structure of multi-neuron firing patterns in primate retina. *J Neurosci*, 26:8254–8266, 2006.
- [3] S. Nirenberg, S. Carcieri, A. Jacobs, and P. Latham. Retinal ganglion cells act largely as independent encoders. *Nature*, 411:698–701, 2001.
- [4] S. H. DeVries. Correlated firing in rabbit retinal ganglion cells. *J. Neurophysiol.*, 81(2):908–920, 1999.

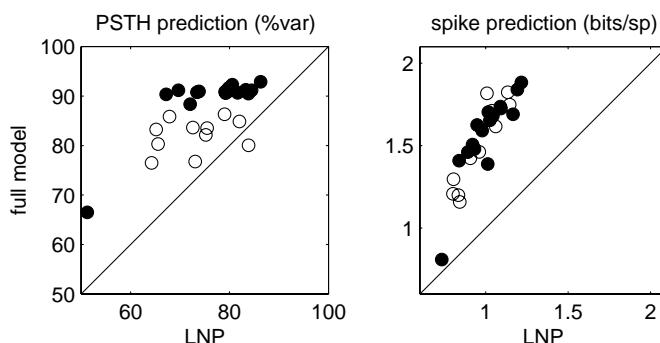


**Figure S10:** Comparison of predictive power of full model and an inhomogeneous Poisson (LNP) model, which lacks both coupling and post-spike waveforms, and whose output is therefore a Poisson process (c.f. fig. 3c-d in the main text; same conventions apply). The LNP model performs less accurately than the models with spike history effects, as measured both by the PSTH variance accounted for (left) and the log-likelihood of the observed spike data (right) [7].

- [5] H. Plesser and W. Gerstner. Noise in integrate-and-fire neurons: From stochastic input to escape rates. *Neural Computation*, 12:367–384, 2000.
- [6] E. J. Chichilnisky. A simple white noise analysis of neuronal light responses. *Network: Computation in Neural Systems*, 12:199–213, 2001.
- [7] J. W. Pillow, L. Paninski, V. J. Uzzell, E. P. Simoncelli, and E. J. Chichilnisky. Prediction and decoding of retinal ganglion cell responses with a probabilistic spiking model. *The Journal of Neuroscience*, 25:11003–11013, 2005.
- [8] L. Paninski, J. W. Pillow, and J. Lewi. Statistical models for neural encoding, decoding, and optimal stimulus design. In P. Cisek, T. Drew, and J. Kalaska, editors, *Computational Neuroscience: Theoretical Insights Into Brain Function*, Progress in Brain Research. Elsevier, 2007.
- [9] N. C. Rust, O. Schwartz, J. A. Movshon, and E. P. Simoncelli. Spatiotemporal elements of macaque v1 receptive fields. *Neuron*, 46(6):945–956, 2005.
- [10] E. P. Simoncelli, L. Paninski, J. Pillow, and O. Schwartz. Characterization of neural responses with stochastic stimuli. In M. Gazzaniga, editor, *The Cognitive Neurosciences*, pages 327–338. MIT Press, 3rd edition, 2004.